

Low field vortex matter in YBCO: an atomic beam magnetic resonance study

Harald Hauglin

*Department of Physics, University of Oslo,
PO Box 1048 Blindern, 0316 Oslo, Norway*

Nathan G. Woodard, Samuel Dapore-Schwartz and Gregory P. Lafyatis

Department of Physics, The Ohio State University, Columbus, OH 43210-1106

(Dated: September 5, 2002)

Abstract

We report measurements of the low field structure of the magnetic vortex lattice in an untwinned YBCO single-crystal platelet. Measurements were carried out using a novel atomic beam magnetic resonance (ABMR) technique. For a 10.7 G field applied parallel to the c -axis of the sample, we find a triangular lattice with orientational order extending across the entire sample. We find the triangular lattice to be weakly distorted by the a - b anisotropy of the material and measure a distortion factor, $f = 1.16$. Model-experiment comparisons determine a penetration depth, $\lambda_{ab} = 140 (\pm 20)$ nm. The paper includes the first detailed description of the ABMR technique. We discuss both technical details of the experiment and the modeling used to interpret the measurements.

I. INTRODUCTION

Considerable theoretical and experimental effort has been devoted to better understanding magnetic flux vortices and magnetic vortex /flux-line lattices in superconductors. This activity has been driven by physical phenomena that have been predicted and observed in high- T_C materials and the practical importance of the role the vortex lattice plays in achieving large critical currents in the presence of magnetic fields. Existing techniques for imaging vortices provide largely complementary information. Bitter decoration can produce a one-time map of vortex locations for many types of material in fields of up to a few hundred Gauss, provided the vortices do not move[1]. Scanning tunneling microscopy can show the structure of individual vortices and the vortex lattice but is limited to studying atomically flat samples with very clean surfaces[2, 3]. Electron holography can image the structure and motion of the flux-line lattice in small fields, also for special, thin, flat samples[4]. Real time magneto-optical vortex imaging[5], has so far only been demonstrated in conventional type II superconductors in weak applied fields. Scanning Hall Probe Microscopy can image quasi-static vortex structure in weak fields[6]. Bending [7] has recently reviewed local probes of vortices. Small angle neutron scattering can yield precise information about the lattice structure in the *bulk* of a sample but often requires long integration times and large sample volumes [8].

In a recent paper[9], we demonstrated for the first time a novel “Atomic Beam Magnetic Resonance” technique (abbreviated, “ABMR,” below) for studying magnetic vortices and flux-line lattices. Very recently, we have used this technique to study the vortex matter phase diagram of YBCO very near T_C .[10] The basic idea — illustrated in Fig. 1 — is to allow an atomic beam to skim across the surface of a superconducting sample and measure the rate that rf magnetic resonance (hyperfine) transitions are excited in atoms as they pass over the sample’s flux-line lattice. Transitions are resonantly driven in atoms where the atom’s velocity and the spacings of vortices along its path combine to make an oscillating magnetic field component at the magnetic resonance frequency. Experimentally, we measure the excitation probability for atoms *as a function of their velocity* and work backwards to infer spatial characteristics of the flux-line lattice. Below, we show that, in the weak excitation limit, our measured signal is proportional to the spatial Fourier transform of lattice’s autocorrelation function.

This paper presents and discusses new ABMR measurements made on vortex lattices in a detwinned single-crystal YBCO sample. In addition, this paper presents, for the first time, details of the ABMR experimental technique: we discuss technical aspects of the apparatus and develop the theory and modeling used to interpret results. We begin in Section 2 with an overview. The aim here is to lay out, succinctly, the *essential* physics of the measurements in the context of studying vortex lattices. The atomic physics details needed for accurate quantitative modeling are left for later sections. We show representative experimental data, and draw conclusions immediately, *without* sophisticated modeling. In section 3 we describe the apparatus and discuss technical details that may affect the measurements. Section 4 contains the theoretical basis of the technique and derives a two-level Master equation model that we have found invaluable in interpreting experimental results. Section 5 compares the experimental data with model predictions to develop a *detailed* description of the vortex lattice.

II. OVERVIEW

The idea behind our experimental approach was originally suggested by Brown and King in the early 1970s. [11] We skim a thermal beam of atomic potassium, mostly ^{39}K , across the vortex lattice of a superconducting sample. The lowest electronic state of ^{39}K , the $4s$ state (Fig. 2) has two hyperfine levels $F = 1$ and $F = 2$ separated by $\Delta E/h \equiv f_0 = 462$ MHz. An oscillating magnetic field at that frequency will resonantly drive transitions between these two levels. A ^{39}K atom in the $F = 1$ level, travelling through the *spatially inhomogeneous* magnetic field just above the surface of a type II superconductor in the mixed state sees a *time-dependent* magnetic field that depends on the atom's velocity and the spatial pattern of vortices in the superconductor. If the frequency spectrum of that field has a component at 462 MHz, transitions to the $F = 2$ level will be resonantly driven. Atoms with different velocities are sensitive to different *spatial* periodicities of the vortex lattice magnetic field. As an example, an atom with a velocity of 462 m/s — a typical velocity for an atom in a thermal potassium beam — will be excited by vortices spaced 1 μm apart, the typical nearest neighbor distance for the vortex lattice with a flux density of about 20 G. *Experimentally*, we measure the excitation probability for atoms as a function of their velocity and use that measurement to identify important length-scales in the vortex

lattice.

The essential experimental operations, then, are: (1) preparing atoms in the initial hyperfine level; (2) passing atoms over the vortex lattice of a superconducting sample, and; (3) detecting the fraction of atoms excited as a function of velocity.

We carry out these out as follows (see Fig. 3): (1) The atomic beam is prepared by optically pumping all atoms to the $F = 1$ level of the electronic ground state — the initial level of the 462 MHz magnetic resonance transition. (2) 1 meter downstream, atoms pass over the surface of a superconductor where vortices may drive the 462 MHz magnetic resonance transition. Atoms travel along the superconductor’s surface for a distance of about a millimeter. Our modelling indicates that only those passing within $1\ \mu\text{m}$ of the surface are significantly excited. (3) Atoms excited by the vortex lattice are detected using laser induced fluorescence from an optical transition out of the $F = 2$ “final” hyperfine level. The Doppler shift between the atomic optical transition and the laser tuning allows a specific velocity-class of atoms to be excited and a data run consists of progressively tuning into resonance and measuring fluorescence for the different velocity-classes of atoms in the atomic beam.

Fig. 4 and Fig. 5 show representative data taken for vortex lattices created in a single-crystal detwinned YBCO platelet. The sample was cooled through its superconducting transition in the presence of a weak bias field (“field-cooled”). For these data, the direction of the bias field is perpendicular to the superconductor. This is the YBCO sample’s crystalline c -axis and the z -axis in the analysis below. The atomic beam passes over the sample parallel to the a -axis of the crystal, our “ x -axis.” To identify important lengths in the vortex lattice, we display the measured excitation probability as a function of the length scale,

$$l = \frac{v}{f_0}, \quad (1)$$

for which a given atom velocity, v , is sensitive. In Fig. 4 we show a series of measurements taken for different bias fields and observe the expected qualitative trend — as the field is increased, the vortices become more tightly packed.

Sometimes, *structural* information may be immediately extracted from measurements. Fig. 5 shows data taken at 10 K after “field cooling” the sample in a 12 G bias field. Below, we show how these data, through comparisons with model predictions, can provide a detailed picture of the vortex lattice. Here, we will take a less formal look at the measurements.

Decoration experiments by Dolan et al [12] have found that triangular vortex lattices form in YBCO samples with the lattice slightly distorted by being compressed along the a -axis of the crystal. In Fig. 6, we show an undistorted triangular lattice and consider first the ABMR signal that would be expected from it. Now, the strongest peaks in our data are due to periodically spaced rows of nearest neighbor atoms. There are three sets of such rows, as are indicated on the figure. We do not know, *a priori*, the orientation of the vortex lattice with respect to the atomic beam. If they were aligned as shown in Fig. 6A), we would expect a single peak — the periodicity along the atomic beam for the dashed rows is the same as for the dotted rows and the beam travels along those rows indicated by the solid line. Thus, the fact that we see *two* peaks in Fig. 5 indicates that the vortex lattice's orientation is *tilted* with respect to the atomic beam. And the fact that we see *only* two peaks suggests that vortex lattice has the *same orientation* over the entire surface of the sample [13] Fig. 6B) considers this case and the darker bars indicate the principal periodicities seen along the atomic beam. For an angle of tilt, θ , these are found to be:

$$d_1 = \frac{\sin 60^\circ}{\sin(60^\circ - \theta)} d_0 \quad d_2 = \frac{\sin 60^\circ}{\sin(60^\circ + \theta)} d_0 \quad d_3 = \frac{\sin 60^\circ}{\sin \theta} d_0 \quad (2)$$

Where d_0 is the nearest neighbor vortex spacing. The *ratios* of these may be used to find the tilt between the atomic beam and the vortex lattice: for a given tilt, the ratios are independent of the vortex density (i.e. magnetic field) and are unchanged even if the vortex lattice is compressed along the axis of the beam:

$$\frac{d_1}{d_2} = \frac{\sin(60^\circ + \theta)}{\sin(60^\circ - \theta)}$$

Identifying the $1.68 \mu\text{m}$ and $1.24 \mu\text{m}$ peaks in Fig 6 with d_1 and d_2 , respectively, determines that the vortex lattice is tilted 15° from the atomic beam — the crystalline a -axis. The relative orientation of the vortex lattice and the underlying crystalline axes was found to be a robust property: we have made vortex lattices many times in this sample and found the lattice to form *always* oriented the same way. Interestingly, there is *no* immediately obvious connection between the orientation of the vortex lattice and either the underlying crystalline symmetry or the edges of the sample.

The positions of the peaks in Fig. 5 together with the vortex density can be used to determine the *distortion* of the vortex lattice relative to the atomic beam (= a -axis of

the crystalline host in the present case). For an undistorted triangular lattice, the nearest neighbor spacing is $d_0 = \sqrt{2/\sqrt{3}}\sqrt{\phi_0/B}$, where ϕ_0 is the quantum of flux and B is the flux density perpendicular to the surface. Using a miniature Hall probe array we measured the mean field at the surface of the sample and found it to be 10.7 G — uncertainty due to screening by the sample makes this measurement necessary. Now, Eq. 2 predicts that an *undistorted* 10.7 G vortex lattice tilted $\theta = 15^\circ$ with respect to the atomic beam, should produce peaks at $d'_1 = 1.83 \mu\text{m}$ and $d'_2 = 1.34 \mu\text{m}$. However, we measure $d_1 = 1.68 \mu\text{m}$ and $d_2 = 1.24 \mu\text{m}$. Therefore, the vortex lattice in the sample must be compressed along the beam axis (the crystalline a -axis) by $d'_1/d_1 = d'_2/d_2 = 1.08$ and, to produce the correct vortex density, it must be stretched along the b -axis by a corresponding amount. Dolan et al[12] define the distortion factor, f , as the b -axis scaling/ a -axis scaling. In our case, $f = 1.08^2 = 1.16$. This value is consistent with the measurements of Dolan et al[12], who observed distortions ranging from $f = 1.11$ to $f = 1.15$ in the samples they decorated. More recently, the small angle neutron scattering studies of Johnson et al [14] found $f = 1.18$. This value was later corroborated by muon-spin measurements on the same sample that found $f = 1.16$. [15] Both Dolan et al and Johnson et al argue that the distortion factor is equal to the ratio of the penetration depths along the crystalline axes, $f = \gamma_{ab} \equiv \lambda_a/\lambda_b$, and both papers contain discussions that compare with experiments that otherwise measure those penetration depths. Briefly, our value, $f = 1.16$, is somewhat lower than the $\gamma_{ab} = 1.37$ to 1.6 reported in polarized reflectivity measurements [16] and at the low end of the range, 1.2 to 1.8 found in the Josephson tunneling studies of Sun et al.[17] Finally, we note that the third peak predicted by Eq. 2 for the lattice in Fig 5, $d_3 \sim 4.5 \mu\text{m}$, is out of the range of sensitivity of the present experiment.

While crystalline vortex lattices with sample-wide order provide the richest data, *any* vortex arrangement will generate a signal. Fig. 7, for example, shows data acquired from the vortex lattice of a 100 nm thick niobium film in a 13.4 G magnetic field applied perpendicular to the film's surface. The single asymmetric peak — steep on the short distance side, gently sloping on the long distance side — is characteristic of a strongly disordered vortex lattice with only short range translational correlations. These data are analogous to the X-ray diffraction of an amorphous solid. The model-generated curve superimposed on the experimental data is for a vortex lattice with a translational correlation length about 4 times the nearest neighbor spacing[9]. We discuss details of the modeling below. For now, Fig.

8 concludes this overview section with a gallery of model predictions for several different phases of vortex matter.

III. EXPERIMENTAL DETAILS

In this section, we describe the apparatus and discuss technical details important to the measurement. See Fig. 2 and Fig. 3. Initially, a thermal potassium beam is produced in an oven operated at about 400° C. The thermal velocity distribution of the atoms in the beam provides sufficient quantities of atoms to allow measurements for velocities between 200 and 1000 m/s . For the 462 MHz hyperfine transition, these velocities probe distances $\sim 0.5 - 2.5 \mu\text{m}$. A triangular lattice with $0.5 \mu\text{m}$ nearest neighbor spacings corresponds to an 80 G applied field. Thus for studying superconductors, this represents a “low field” diagnostic tool.

A. State Preparation

The ground state, $4s \ ^2S_{1/2}$, hyperfine levels in the thermal atomic beam coming from the oven will be statistically populated. A laser tuned to the 770 nm, $4s \ ^2S_{1/2}(F = 2) \rightarrow 4p \ ^2P_{1/2}(F = 2)$, transition optically pumps almost all of the atoms to the lower ($F = 1$) hyperfine level. A pseudo depolarizer in the pumping laser beam allows all magnetic states of the $4s \ ^2S_{1/2}(F = 2)$ atoms to be moved to the lower level. Typically 99.5% of the atoms wind up in that level.

B. Sample Region

The atoms next pass to a differentially pumped sample chamber. For this work, the sample was a twin-free, single-crystal YBCO platelet with dimensions $0.7 \text{ mm} \times 1.7 \text{ mm} \times 0.1 \text{ mm}$. It was grown by a self-flux method[18] at the Ohio State University. It has a sharp superconducting transition ($\Delta T = 0.3 \text{ K}$) with an onset at $T_C = 93.0 \text{ K}$. The sample was thermo-mechanically detwinned in an oxygen atmosphere using a platinum anvil similar to the apparatus in ref. [19].

The sample was mounted to a copper stage that in turn was attached to an LHe reservoir via a thermally resistive stainless steel link. The stage’s temperature was measured with a silicon thermometer and could be varied from 5 K to >100 K using a resistive heater. To reject those atoms that pass too far from the sample to contribute to the signal but close enough to contribute to the background in the detector, a tunnel shaped fixture was mounted above the sample that served as an aperture for the atomic beam. This aperture extended the length of the sample along the beam and allowed through only those atoms passing within $2\text{ }\mu\text{m}$ of the sample’s surface. Low resistance, $R < 0.1\Omega$, leads were mounted to the sample in a 4-wire configuration so that we could measure the sample’s resistance and also drive transport currents through the sample perpendicular to the atomic beam. Three pairs of coils mounted outside of the vacuum system allow us to apply small fields to samples in arbitrary directions.

Immediately following the sample chamber is a Stern-Gerlach magnet that serves the role of a beam stop and dumps *unexcited* atoms from the beam — the “main beam;” This step was included because, otherwise, off-resonance fluorescence from the unexcited atoms caused large backgrounds in the detector. Two side-effects of the Stern-Gerlach magnet are 1) in addition to filtering all out atoms in the $F = 1$, lower level, it also removes from the atomic beam “signal” atoms excited to the $F = 2, M_F = -2$ state and 2) the direction of atoms exiting the magnet depend on their velocity. To send different velocity classes of atoms on to the detector, it is necessary to vary the strength of the Stern-Gerlach magnet.

C. Detector

Experimental difficulties in detecting the small numbers of vortex-lattice-excited atoms as a function of velocity lead to an involved detection scheme. At the heart of the detection system is the “detection laser” that drives resonance fluorescence in atoms that were excited by the vortex lattice. The detection laser is directed nearly antiparallel to the atomic beam and for a given frequency, it excites a velocity class of atoms with $\delta v \sim 20\text{ m/s}$. A portion of the fluorescence is collected by an optical system and detected by a high efficiency detector. In our earlier work, [9] this detector was a photomultiplier tube. For our more recent work we use a large-area avalanche photodiode that is cooled with liquid nitrogen[20]. There is a magnetic field parallel with the laser at the beams’ intersection and the laser light is σ^+

polarized. An important feature of this arrangement is that, while atoms may be excited by the vortex lattice to any of the Zeeman states in the of upper level of 462 MHz transition of, the detection system is especially sensitive to those atoms that end up in the $F = 2$, $M_F = +2$ state . An atom in this state is driven by the laser in a cycling transition: the laser light can excite only to the $M'_F = +3$ of the upper level of the optical transition and this level can decay only back to the $M_F = +2$ state where it may be reexcited, repeatedly. Typically an atom will produce on the order of 200 fluorescence photons of which 40 will be collected and detected.

We found that, despite extensive baffling, the “detection laser” caused large fluctuating scattered light backgrounds in the detector. Phase sensitive (lockin) detection can discriminate against such backgrounds but this requires a modulation of the atomic beam signal. For this reason, a second beam from the 770 nm optical pumping laser was directed across the atomic beam just after the Stern-Gerlach magnet. This second pumping laser beam returns excited atoms to the lower level of the 462 MHz transition thus turns off the signal at the detector. We mechanically chopped the second pumping laser beam at a frequency of 140 Hz. This suitably chopped the signal at the detector and allowed us to carry out lockin detection at that frequency.

Since our initial work [9], we have added a stage that transfers vortex-lattice-excited (signal) atoms from other $F = 2$ magnetic substates into the $M_F = +2$ state for which the detection system is most sensitive. Doing this both increases the signal and provides better defined the experimental conditions for quantitatively interpreting results. The latter is because the M_F states individually fluoresce at slightly different frequencies. Without this step, it is conceivable that structure in the detected signal could be due to the Zeeman structure of the detection transition and *not* structure in the vortex lattice. In addition, knowing that all vortex-lattice-excited atoms contribute identically to the fluorescence signal considerably simplifies the quantitative analysis and modeling of the experiment. To implement this operation, just upstream of the detector, see Fig. 3, the atomic beam is crossed transversely by a beam picked off the detection laser. That beam is σ^+ polarized. A weak (~ 2 G) magnetic field is oriented along the laser beam to define a quantization axis. As atoms scatter photons from this laser, they are moved toward higher M_F states with the net result that $> 90\%$ of the vortex lattice excited atoms in $M_F = -1, 0, 1$ Zeeman states are moved to the $M_F = 2$ state and detected.

D. Data Acquisition

Data acquisition consists of measuring fluorescence as a function of velocity for the atoms excited by the vortex lattice. Two parts of the detection scheme have velocity sensitivity: the Stern-Gerlach magnet's steering and the Doppler shifted resonance frequency of the atoms' optical transition. To take data, these must be changed synchronously. To make the laser resonant *with a particular velocity class* of atoms, it is most convenient to keep the laser itself locked to a single frequency and to tune the atomic transition into resonance using the Zeeman effect. The detector magnet provides the required field. Data are acquired by changing in step the currents to the Stern-Gerlach magnet and the detector magnet while measuring the avalanche photodiode current using a lockin amplifier that is referenced to the chopped second pumping beam. Typically, a data set consists of fluorescence recorded for 1000 points (velocities) and takes 30 seconds to acquire.

To measure the excitation *probability* as a function of velocity, we proceed as follows. (1) The sample is warmed to a temperature above T_c where there is no vortex lattice and data are recorded. This gives a warm pumped data set, WP, and shows how effective the initial state preparation is. (2) The sample is then allowed to cool in an applied magnetic field. For each temperature of interest, we record two fluorescence distributions: The raw 'cold pumped,' CP signal, and the 'cold unpumped,' U signal that we get by blocking the first pumping beam. The latter serves as a reference for the measurement, since the strength of the fluorescence signal in this case corresponds to the intensity of the atomic beam coming from the oven.

The signals are smoothed by performing a 20 point running average of the raw data and are reduced by subtracting the warm pumped data WP from the cold pumped signal CP and dividing by the unpumped distribution U. This procedure is shown in Fig. 9 for a representative set of data. Note that this way of normalizing the experimental magnetic resonance profiles automatically measures the *absolute* excitation probability caused by the vortex lattice.

IV. MODELING

We interpret our experimental results by comparing our measurements with theoretical signals predicted for likely vortex lattices. To predict signals we require two theoretical inputs. First we need the relation between the structure of a vortex lattice in a sample and the magnetic field above the sample's surface; Second, we need to determine the excitation of a atom due to the time-dependent magnetic field it sees as it passes through the field of the vortex lattice.

A. The field of a vortex lattice

The magnetic field above the sample surface may be found by solving the London-Maxwell equations with the appropriate boundary conditions. Marchetti [21] found that for a bias field applied parallel to the major anisotropy ($\hat{\mathbf{c}}$) axis of a sample, the partial spatial Fourier transform — over x and y directions — of the magnetic field at a distance z above the sample surface is given by

$$\mathbf{B}(\mathbf{q}, z) = \left[\frac{\phi_0}{\lambda_{ab}^2} \frac{(\hat{\mathbf{z}} - i\hat{\mathbf{q}})e^{-qz}}{\alpha(\alpha + q)} \right] \sum_l e^{i\mathbf{q} \cdot \mathbf{R}_l}, \quad (3)$$

where

$$\alpha = \sqrt{q_x^2 + q_y^2 + \frac{1}{\lambda_{ab}^2}}, \quad (4)$$

$\{\mathbf{R}_j\}$ are the positions of the vortices at the sample's surface, $\lambda_a, \lambda_b, \lambda_c$, are the magnetic penetration depths along the crystalline a-, b- and c-axis, $\lambda_{ab} = \sqrt{\lambda_a \lambda_b}$, $\gamma = \lambda_c / \lambda_{ab}$, $\mathbf{q} = (q_x, q_y)$, $\phi_0 = 20.7 \text{ G}(\mu\text{m})^2$ is the flux quantum, and $\hat{\mathbf{z}}$ and $\hat{\mathbf{q}}$ are unit vectors.

B. Excitation of Atoms by the vortex field

Next, we consider the excitation of a potassium atom by the fluctuating field, $\mathbf{B}(t)$, in its rest frame as it passes over a vortex lattice. Relevant atomic structure is shown in Fig. 2. Initially, the atomic beam is optically pumped to the $F = 1$ level and we expect that the magnetic states of this level will be equally populated at the beginning of a measurement.

We consider the excitation of atoms to magnetic states of the $F = 2$ level. The interaction Hamiltonian of an atom in a time varying magnetic field is:

$$H'(t) = -\boldsymbol{\mu} \cdot \mathbf{B}(t) \quad (5)$$

here $\boldsymbol{\mu}$ is the magnetic dipole moment operator of the atom. For a ground state potassium atom, the electron has no orbital angular momentum and the magnetic moment of the nucleus is negligibly small, so the magnetic dipole moment operator is just that of the valence electron's spin: $\boldsymbol{\mu} = -2\mu_B \mathbf{S}$; where μ_B is the Bohr magneton and \mathbf{S} is the dimensionless electron spin operator. Expressing the magnetic field in terms of its spherical components: $B_{\pm 1} = (B_x \pm iB_y)/\sqrt{2}$ and $B_0 = B_z$, gives:

$$H'(t) = 2\mu_B \sum_{j=-1,0,1} (-1)^j S_j B_{-j}(t) \quad (6)$$

The general problem of the effect of an arbitrarily varying magnetic field on an arbitrary mixture of states in the $4s$ manifold is difficult. We have carried out a limited number of calculations by solving the full time-dependent Schrödinger equation using this Hamiltonian in which $\mathbf{B}(t)$ is found by following specific paths over a candidate vortex lattices. These calculations are extremely time consuming and generally obscure the physics essential to the excitation process. These calculations are carried out to check the reliability of the approach that we usually use and which is described next.

We begin by using first order perturbation theory to find the sample-averaged excitation rate of the $F'' = 1 \rightarrow F' = 2$, hyperfine transition for an atom with a given velocity and height traveling above the superconductor. Here, the convention is that double primed variables refer to the energetically lower state of a transition and single primed variables refer to the energetically higher state. We take as a basis the hyperfine (variables=electronic spin, nuclear spin) energy eigenstates for the mean field that we measure at the sample's surface. The quantization axis is given by this field — i.e. is perpendicular to the sample surface. The magnetic resonance transition is a magnetic dipole transition with selection rules $\Delta M_F = \pm 1, 0$ and thus within first order perturbation theory, the problem of excitation by the vortex lattice of the initial, $F'' = 1$ level, reduces to nine uncoupled two-state problems corresponding to the nine allowed $M_F'', F'' = 1 \rightarrow M_F', F' = 2$ transitions.

In Appendix 1, we derive the first order perturbation result for the excitation rate between specific Zeeman states. For atoms with velocity, v , traveling a height, z , above the sample,

$R_{ge}(v, z)$, the rate of excitation from the Zeeman state, g , in the ground state manifold, to e in the excited state manifold is given by:

$$R_{ge}(v, z) = 2\eta_j |M_{eg}|^2 \frac{1}{\pi v} \frac{B\phi_0}{\lambda_{ab}^4} \left(\frac{\mu_B}{\hbar}\right)^2 \int_{-\infty}^{+\infty} dq_y \frac{e^{-2qz}}{[\alpha(\alpha + q)]^2} S_2(\mathbf{q}), \quad (7)$$

Where $\eta_j = 1$ for $\Delta M_F = 0$ transitions and $\eta_j = \frac{1}{2}$ for $\Delta M_F = \pm 1$ transitions. M_{eg} is a transition (electron-spin) matrix element; B , is the mean magnetic field (\approx the applied field) at the sample's surface; and N , is the total number of magnetic vortices in the sample. Most importantly, $S_2(\mathbf{q}) = (1/N) \left| \sum_j \exp(i\mathbf{q} \cdot \mathbf{R}_j) \right|^2$ is the vortex lattice “structure factor.” We also define a *level-to-level* excitation rate, $R_{GE}(v, x)$, by summing Eq. 7 over (Zeeman) final states and averaging over initial states:

$$R_{GE}(v, x) = \frac{1}{3} \sum_{g,e} R_{ge}(v, z) \quad (8)$$

Here, the upper case letters, G , and E , refer to the ground and excited *levels*, respectively.

We jump ahead a little and show in Fig. 10 *first order perturbation theory* predictions for the excitation probabilities of atoms passing at different heights above the 10.7 G vortex lattice discussed previously. These curves were generated by multiplying the rates of Eq. 8 by the time it takes an atom with the given velocity to pass over the sample. This particular figure used a structure factor that yields a good fit with our measurements, though, at this point the details of the calculation are unimportant and we are using the figure to illustrate a couple of general features. Specifically (1) the actual signal from the experiment is due to atoms passing extremely close to the sample's surface — atoms passing at heights over $1 \mu\text{m}$ are negligibly excited. And (2) the simple perturbation theory treatment “predicts” excitation probabilities greater than unity for atoms that pass close to the sample. This indicates that for some heights, the transitions are saturated and it is necessary to go beyond first order perturbation theory and include saturation in our description of the excitation process.

In analyzing the experiment, those atoms passing *extremely* close to the surface would seem to be problematic for an even deeper reason. Very close to the sample's surface, the magnetic field varies widely and treating the fluctuating field due to the vortices as a perturbation on top of the nominal bias field at the surface is not justified. Fortunately,

these atoms do not contribute to the signal, but rather are pulled into the sample by van der Waals forces. We include the van der Waals force in our modeling by using it to provide a lower cutoff to heights above the sample included in predicting signals. This cutoff is on the order of $0.2 \mu\text{m}$ and depends on the atoms' velocity. Still, referring to Fig. 10 even with a lower cutoff of $0.2 \mu\text{m}$, saturation effects are seen to be important.

We use a Master Equation approach to include saturation in our model. As an atom crosses the sample, the probability of its excitation by the vortex lattice to a state e in the $F = 2$ manifold is assumed to satisfy the differential equation (Master Equation):

$$\frac{dP_e(v, z, t)}{dt} = \sum_{g'} R_{g'e}(v, z) [P_{g'}(v, z, t) - P_e(v, z, t)] \quad (9)$$

Where the sum is over the $F = 1$ states, $R_{g'e}(v, z)$ is given by Eq. 7 and we have used the fact that the state-to-state *excitation* rate is equal to the corresponding *deexcitation* rate. Corresponding equations describe the occupation probability of the lower, $F = 1$ states. The excitation probability for an atom is readily found by integrating these (eight) coupled equations for the time the atom is over the sample with the condition that when the atom initially encounters the sample, $P_g(v, z, t = 0) = 1/3$ for each of the three $F = 1$ states. For our experimental conditions, intra-level transitions — e.g. transitions between states in the ground level — should be weak.

Cohen-Tannoudji et al.[22] discuss the justification of the Master Equation approach in describing radiative processes (Einstein A and B coefficients) and much of that discussion is readily adaptable to the present case. In particular, a “coarse graining” of the excitation process allows using a rate coefficient to describe coherent excitation. The basic idea is that the net excitation consists of sum coherent excitations that are, individually, independent of one another — they add incoherently. To carry out “coarse graining” in the vortex-lattice-excitation-of-atoms problem, the coherence time, τ_{coh} , of the vortex-lattice field that excites the atom needs to be much shorter than, τ_{ex} , the time it takes that field to coherently excite the atom. In other words, an atom should be only weakly excited ($\Delta P_e \ll 1$) during the time it travels over the sample a distance equal to the translational correlation length of the vortex lattice. For even the most strongly excited atoms that contribute to the signal (i.e. those at the lower cutoff height), this condition is met.

Additionally, using Eq. 7 for transition rates in the Master Equation(s) *implicitly* assumes

that the vortex lattice is homogenous across the entire sample. For example, if the sample's vortex lattice *actually* consisted of two large domains with very different (local) structure factors, our treatment would need to be extended. Specifically, we assume that the vortex driven excitation *rate*, $R_{g'e}(v, z)$ (coarse-grained — averaged over distances large compared to the vortex lattice translational correlation length) is uniform across the sample. In our work, the most likely violation of this condition results from edge effects. We experimentally investigated this issue by making magneto-optic images of the flux density of the sample and we know from micro hall array measurements, that, for the conditions of Fig. 5, the flux density at the surface is uniform to within a couple of per cent across for the central 2/3's of the sample (it is slightly lower near the sample edges). Of course, even uniformity of the field across the sample, does not *necessarily* mean the vortex lattice itself is homogenous.

For the results presented in this paper, we treat the Zeeman states within the hyperfine levels individually to first order. This is important since the Zeeman shift of the hyperfine states broadens as well as shifts the 'average' $F = 1 \rightarrow F = 2$ transition. In order to account for saturation, we generalize Eq. 9 to the extent possible and work with a single, level-to-level Master equation,

$$\frac{dP_E(v, z, t)}{dt} = R_{GE}(v, z) \left[P_G(v, z, t) - \frac{3}{5}P_E(v, z, t) \right] = R_{GE}(v, z) \left[1 - \frac{8}{5}P_E(v, z, t) \right]. \quad (10)$$

This two-level Master equation is the principal result of the section. Here, $R_{GE}(v, z)$ is the level-to-level transition rate, Eq. 8, P_E and P_G , are the occupation probabilities of the *levels* (summed over the Zeeman states) and the $\frac{3}{5}$ factor insures that for strong saturation, the levels will be statistically populated according to their degeneracies. Note: while Eq. 10 follows from Eqs. 8 and 7 in the unsaturated and strongly-saturated limits, for the general case, this rate equation for the levels *cannot* be *rigorously* derived from the system of rate equations linking the individual states. However, we have made several comparisons between this model and the full solution of the Schrödinger Eq. and generally find agreement to much better than 10%. Fig. 11 shows one such comparison. Importantly, the model results require less than 1/1000th the computer time of the Schrödinger equation solutions. We conclude that, for the purpose of comparing with our measurements, the two-level Master equation model based on Eq. 10 provides an adequate description of the excitation process.

C. Modeling the structure factor

We showed in the previous section that the atomic beam signal is intimately related to the two-dimensional structure factor, $S_2(\mathbf{q}) = (1/N) \left| \sum_{l=1}^N e^{i\mathbf{q} \cdot \mathbf{R}_l} \right|^2$, for an array of N vortices at positions $\{\mathbf{R}_l\}$. The purpose of this section is to develop a general framework for describing the structure factor for a wide range of potential vortex lattices. For a homogeneous system, $S_2(\mathbf{q})$ can be expressed as [23]

$$S_2(\mathbf{q}) = 1 + \int d^2r e^{i\mathbf{q} \cdot \mathbf{r}} f(\mathbf{r}), \quad (11)$$

where $f(\mathbf{r})$ is the probability distribution for finding a pair of vortices separated by a distance \mathbf{r} . The normalized pair distribution function is $g(\mathbf{r}) = f(\mathbf{r})/n$, where $n = B/\phi_0$ is the average number density of vortices. In the following, we model the distribution function $f(\mathbf{r})$ for a lattice spanned by the primitive vectors \mathbf{r}_1 and \mathbf{r}_2 , and assume that vortex displacements relative to perfect crystalline order is described by a Gaussian distribution. See Fig. 12. We write

$$f(\mathbf{r}) = \sum'_{l,m} \frac{1}{2\pi\sigma(r_{lm})^2} \exp\left(-\frac{(\mathbf{r}-l\mathbf{r}_1-m\mathbf{r}_2)^2}{2\sigma(r_{lm})^2}\right), \quad (12)$$

where $r_{lm} = |l\mathbf{r}_1 + m\mathbf{r}_2|$ and the sum runs over l and m except $l = m = 0$. The Fourier transform of $f(r)$ is evaluated and the structure factor is

$$S_2(\mathbf{q}) = 1 + \sum'_{l,m} e^{-i\mathbf{q} \cdot (l\mathbf{r}_1 + m\mathbf{r}_2)} e^{-q^2\sigma(r_{lm})^2/2}. \quad (13)$$

Here the functional form of the displacement $\sigma(r)$ is used to parametrize the range and magnitude of correlations in the vortex array. In this work we have used a displacement of the form

$$\sigma(r) = \sigma_0(r/a_0)^p, \quad (14)$$

where $a_0 = \sqrt{\phi_0/B}$ is the average vortex separation. For the numerical evaluation of $S_2(q)$ from expression 13, one has to sum over a sufficiently large lattice in order to ensure convergence.

So far we have only included positional disorder in the expression for the structure factor. For the subsequent analysis, we also include orientational disorder by averaging the structure factor over different orientations of the unit cell spanned by \mathbf{r}_1 and \mathbf{r}_2 . In practice this is done

by computing $S_2(q)$ for a particular \mathbf{r}_1 and \mathbf{r}_2 and then averaging over orientations with a Gaussian distribution with a standard deviation $\Delta\theta$ around 0° , i.e. the orientationally averaged structure factor is

$$\overline{S}_2(\mathbf{q}) = \frac{1}{\sqrt{2\pi}\Delta\theta} \int_{-\infty}^{+\infty} d\theta S_2(\mathbf{q}'(\theta)) \exp\left(-\frac{\theta^2}{2(\Delta\theta)^2}\right), \quad (15)$$

where $\mathbf{q}'(\theta)$ is the wave vector \mathbf{q} rotated an angle θ .

The model for $S_2(\mathbf{q})$ as outlined above in expressions (13) — (15) provides a quite general framework for describing different classes of disorder, ranging from crystalline long range order ($p = 0, \Delta\theta = 0$), via powder correlations ($p = 0, \Delta\theta \rightarrow \infty$) and hexatic order ($p = 0.5, \Delta\theta \ll \pi/6$) to isotropic liquid-like order ($p = 0.5, \Delta\theta \rightarrow \infty$). The main fitting parameters are the nearest neighbor displacement σ_0 , the exponent p and the orientational disorder $\Delta\theta$. The penetration depth is sometimes taken as a free parameter and other times fixed using values in the literature.

V. FORMAL ANALYSIS OF VORTEX CORRELATIONS IN YBCO: A CASE STUDY

Next, we use the modeling framework for a quantitative analysis of the vortex lattice correlation in a high quality YBCO single crystal. Comparison between model predictions and experimental data enables us to extract information on the overall symmetry and orientation of the vortex array, the range and magnitude of vortex correlations, and the London penetration depth, λ_{ab} .

We reconsider the data shown in Fig. 5. Formally, we *assume* that the vortex lattice is accurately described by a single, sample-wide autocorrelation function and does *not*, for example, consist of two different domains. Note: this also ignores possible edge effects. We further *assume* that the underlying vortex lattice in the sample, ignoring disorder, can be described by two primitive lattice vectors, \mathbf{r}_1 and \mathbf{r}_2 , as discussed above. This is a much weaker assumption than in the Overview (Section 2) where we restricted consideration to triangular lattice variants. For example, if the vortex lattice *actually* had square or rectangular symmetry, we would discover this fact in the course of the present analysis.

A fit to the data proceeds at two levels: i) The overall symmetry and orientation of the vortex lattice unit cell (Fig.13) is determined by the two length scales of the ABMR

peaks *and* their relative intensities. ii) The shape and strength of the ABMR signal contain information on the magnitude and range of the vortex correlation function, as well as the penetration depth λ_{ab} . We retrieve that information by comparing model predictions for various putative correlation functions with the experimental data. Note that the vortex array correlation *cannot* be extracted by simple curve-fitting to the diffraction peaks, in contrast to neutron diffraction data, since the peaks are *broadened* due to saturation of the ABMR transitions (section 4.2). For the same reason, there is no simple analytic relation between the penetration depth and the total signal strength.

We consider the oblique unit cell specified by the magnitudes of the primitive lattice vectors, \mathbf{r}_1 and \mathbf{r}_2 , the angle θ that \mathbf{r}_1 makes with the atomic beam direction (x-axis) and the angle β between \mathbf{r}_1 and \mathbf{r}_2 . These four parameters have to satisfy the following criteria: a) The two shortest projected lattice row spacings, d_1 and d_2 in Fig. 13, have to equal the ABMR peak positions $1.24 \mu\text{m}$ and $1.68 \mu\text{m}$. b) The unit cell area be correct, $r_1 r_2 \sin \beta = \phi_0 / B$. And c) The unit cell has to reproduce the relative intensities of the two ABMR peaks. This last criterion is less “absolute” than a) and b) in the sense that the interdependencies it imposes on the lattice parameters depends, weakly, on the chosen model of disorder. The best-fit-model vs. data comparison is shown in Fig. 13. The unit cell is described by $r_1 = 1.4 \mu\text{m}$ and $r_2 = 1.6 \mu\text{m}$ at an angle $\beta = 62^\circ$. The shortest primitive lattice vector, \mathbf{r}_1 , is rotated an angle $\theta = 18^\circ$ with respect to the crystalline a-axis of the sample. These results are consistent with the less formal discussion in the overview of section 2.

A fit to the shape and overall strength of the ABMR signal uses the modeling framework developed above. For a given set of lattice parameters, we compute the structure factor $S_2(\mathbf{q})$ (Eqs. 13 – 15) parametrized by the displacement relative to perfect order $\sigma(r) = \sigma_0(r/a_0)^p$, and the angular disorder $\Delta\theta$. The structure factor $S_2(\mathbf{q})$ is used together with the penetration depth λ_{ab} as an input for computing the hyperfine excitation rate coefficients, Eqs. 7, 8 and the transition probability, Eq. 10 as a function of velocity v for a given height z . Finally, the transition probability is averaged over the relevant range of heights. Model predictions are generated for a range of values of the input parameters. The best fit model shown in Fig. 13 is for $p = 0.5 \pm 0.1$, $\sigma_0 = (0.14 \pm 0.01) a_0$, and angular disorder $\Delta\theta \leq 2^\circ$.

Fig. 13 shows that the overall strength of the signal at 10 K is best matched for a penetration depth, $\lambda_{ab} = 140 \pm 20 \text{ nm}$. This is consistent with typical values for the low

temperature penetration depth found by other workers. By combining this result with the the distortion factor found in section 2, our measurements independently provide estimates of the individual penetration depths, $\lambda_a = 151 \pm 20$ nm and $\lambda_b = 130 \pm 20$ nm. These values are virtually identical to those deduced from Johnson et al's[14] small angle neutron scattering work, $\lambda_a = 150$ nm and $\lambda_b = 127$ nm, though given the error bars of our measurements, the level of agreement is somewhat fortuitous. Similarly, our values are in harmony with the polarized light scattering measurements of Wang et al,[16] $\lambda_a = 160$ nm, $\lambda_b = 117$ nm and appear consistent with the Josephson-tunneling results of Sun et al,[17] who report values for $\lambda_a = 161$ to 270 nm and $\lambda_b = 90$ to 174 nm for several different samples.

VI. CONCLUDING REMARKS

We conclude with some general observations about the ABMR technique, itself.

The strengths and weaknesses of the ABMR are largely complementary to those of other imaging-type vortex lattice diagnostic tools. Weaknesses include, in contrast to neutron diffraction measurements, the technique directly provides only 1-D information, it probes vortices only at a superconductor's surface and as currently implemented it is restricted to relatively low fields. In contrast with decoration experiments or electron holography, the atomic beam technique provides sample averaged information about the vortex lattice: it cannot look at individual vortices or even domains within the vortex lattice.

On the positive side, some cases — e.g. isotropic lattices or lattices with sample-wide order — the 1-D measurement can lead to a 2-D description of the vortex lattice. The atomic beam technique does *not* require especially thin or especially smooth samples. Nor does it require a large quantity of sample material — c.f. neutron diffraction studies. In contrast to the “one-shot” nature of decoration experiments and the heroic integrations sometimes required for neutron diffraction measurements, atomic beam measurements are made in near-real time and can follow the evolution of a vortex lattice on a time scale of minutes. Measurements are possible in the presence of transport currents and are possible even if vortices are moving. Finally, to date, it is the *only* imaging-type diagnostic tool that has had sufficient sensitivity to study vortex lattices near T_c [10].

In many ways, atomic beam technique is similar to neutron diffraction. Both provide information on the vortex lattice in k -space. Both provide sample-averaged information.

The discussion leading up to Eq. 7 is very similar to that needed to predict and analyze signals from neutron diffraction experiments. [8] Signal strengths for both types of experiments (to first order) $\sim \lambda_{ab}^{-4}$. Approaching T_c from below, the penetration depth diverges and for both neutron diffraction and AMBR experiments this leads to sharply decreasing signals and increasingly difficult measurements. Why is it that the atomic beam method is able to make measurements near T_c ? The sensitivity of the atomic beam method relative to neutron diffraction is a consequence of the fact that in the atomic beam method, the signal is produced by the interaction of the Bohr magneton of an atom's valence electron with the vortex lattice field. In neutron diffraction, it is the much smaller nuclear magneton-magnetic field interaction that generates the signal.

We gratefully acknowledge the technical assistance of John Spaulding, the OSU model shop, and Jeff Fox and useful discussions with Tom Lemberger. We thank Mike McElfresh/Eli Zeldov for providing the Hall array. This work was supported by the PYI program of NSF and the MISCION program of DOE. HH acknowledges support from the University of Oslo and the Norwegian Research Council.

VII. APPENDIX: EXCITATION RATE COEFFICIENT FOR AN ATOM OVER A VORTEX LATTICE

For our models we need to find the sample-averaged excitation rate $F = 1 \rightarrow F = 2$ of an atom with a given velocity and height traveling above vortex lattice. We begin with the first order perturbation theory calculation of excitation out of the $F = 1$ level. We take as a basis the hyperfine (variables=electronic spin, nuclear spin) energy eigenstates for the mean field that we measure at the sample's surface. The quantization axis is given by this field — i.e. is perpendicular to the sample surface. The magnetic resonance transition is a magnetic dipole transition with selection rules $\Delta M_F = \pm 1, 0$ and thus within first order perturbation theory, the problem of excitation by the vortex lattice of the initial, $F = 1$ level, reduces to nine uncoupled two-state problems corresponding to the nine allowed $F = 1 \rightarrow F = 2$ transitions. We consider an individual transition between a specific, initial magnetic state, $|g\rangle$, in the lower level and a specific final magnetic state, $|e\rangle$, in the upper level. The interaction Hamiltonian has a non-zero matrix element, $H'_{eg}(t)$, for only one term (at most) of the sum in Eq. 6 and will be driven by only one spherical component of the field. The

transition probability that an atom, initially in $|g\rangle$ is excited to state $|e\rangle$ is to first order in the interaction:

$$P_{ge}^{(1)} = \frac{1}{\hbar^2} \left| \int_{-\infty}^{+\infty} H'_{eg}(t) e^{i\omega_{eg}t} dt \right|^2 \quad (16)$$

$$= 4 \left(\frac{\mu_B}{\hbar} \right)^2 |M_{eg}|^2 \left| \int_{-\infty}^{+\infty} B_{-j}(t) e^{i\omega_{eg}t} dt \right|^2. \quad (17)$$

$$= 4 \left(\frac{\mu_B}{\hbar} \right)^2 |M_{eg}|^2 \left| \int_{-\infty}^{+\infty} B_j(t) e^{-i\omega_{eg}t} dt \right|^2 \quad (18)$$

Here $H'_{eg}(t)$ is the matrix element of the interaction Hamiltonian, $M_{eg} = \langle e | S_j | g \rangle$ is the non-zero electron spin operator matrix element and ω_{eg} is the magnetic resonance transition's frequency, $= 2\pi \cdot 462 \text{ MHz} +$ the transition's Zeeman shift for the average field near the sample's surface. The final result, here, reflects the fact that the excitation probability is proportional to the power spectrum of the field seen by the atom at the resonant frequency of the transition.

For an atom travelling in the x -direction with velocity v , at a height z above the sample's surface and a transverse displacement y from the center of the sample, the *temporal* Fourier transform $B_j(\omega)$ of the magnetic field $B_j(t)$ in the moving reference frame of the atom is related to the *spatial* Fourier transform $B_j(q_x, y, z)$ of the magnetic field $B_j(x)$ along the atomic trajectory in the lab frame:

$$\int_{-\infty}^{+\infty} B_j(t) e^{-i\omega_{eg}t} dt = \frac{1}{v} \int_{-\infty}^{+\infty} B_j(x, y, z) e^{-iq_x x} dx = \frac{1}{v} B_j(q_x, y, z), \quad (19)$$

where $q_x = \omega_{eg}/v$. The distance scale probed by atoms with velocity, v , is $l = 2\pi/q_x = v \cdot 2\pi/\omega_{eg}$. The first order transition probability can now be written:

$$P_{eg}^{(1)} = \frac{4}{v^2} \left(\frac{\mu_B}{\hbar} \right)^2 |M_{eg}|^2 |B_j(q_x, y, z)|^2. \quad (20)$$

Here $B_j(q_x, y, z)$ is understood as the partial Fourier transform of $B_j(x, y, z)$ for a particular trajectory given by y and z . In the actual experiment, we measure the transition probability averaged across a beam's transverse dimensions, y and z . $|B_j(q_x, y, z)|^2$ can be expressed in terms of the 2D Fourier transform $B_j(\mathbf{q}, z)$ of the previous section:

$$|B_j(q_x, y, z)|^2 = \left| \frac{1}{2\pi} \int_{-\infty}^{+\infty} dq_y B_j(\mathbf{q}, z) e^{iq_y y} \right|^2. \quad (21)$$

The average of this quantity across the width of the sample is

$$\frac{1}{L_y} \int dy |B_j(q_x, y, z)|^2 = \left(\frac{1}{2\pi} \right)^2 \frac{1}{L_y} \int_{-L_y/2}^{L_y/2} dy \int_{-\infty}^{+\infty} dq_y \int_{-\infty}^{+\infty} dq'_y B_j(\mathbf{q}, z) B_j^*(\mathbf{q}', z) e^{i(q_y - q'_y)y}. \quad (22)$$

Assuming that L_y is large we use $\int dy e^{i(q_y - q'_y)y} = 2\pi\delta(q_y - q'_y)$ and obtain the average transition probability for atoms travelling at height z ,

$$P_{ge}^{(1)}(q_x, z) = \frac{2}{\pi v^2 L_y} |M_{eg}|^2 \left(\frac{\mu_B}{\hbar}\right)^2 \int_{-\infty}^{+\infty} dq_y |B_j(\mathbf{q}, z)|^2. \quad (23)$$

Including the expression for the magnetic field structure near the sample surface (3), we find the average first order transition probability for atoms travelling near a vortex array with speed v along the x -axis at height z .

$$P_{ge}^{(1)}(v, z) = \eta_j \frac{4 |M_{eg}|^2}{v^2} \left(\frac{\mu_B}{\hbar}\right)^2 \frac{\phi_0^2}{2\pi\lambda_{ab}^4} \frac{1}{L_y} \int_{-\infty}^{+\infty} dq_y \frac{e^{-2qz}}{(\alpha(\alpha + q))^2} \left| \sum_{l=1}^N e^{i\mathbf{q} \cdot \mathbf{R}_l} \right|^2, \quad (24)$$

Where $\eta_j = 1$ for $\Delta M_J = 0$ transitions in Eq. 6 and $\eta_j = \frac{1}{2}$ for $\Delta M_J = \pm 1$ transitions. Rewriting this in terms of the two-dimensional vortex array structure factor, $S_2(\mathbf{q}) = (1/N) \left| \sum_j \exp(i\mathbf{q} \cdot \mathbf{R}_j) \right|^2$ (note: the structure factor is, to within a constant, the Fourier transform of the vortex lattice autocorrelation function):

$$P_{ge}^{(1)}(v, z) = 2\eta_j |M_{eg}|^2 \frac{L_x}{\pi v^2} \frac{B\phi_0}{\lambda_{ab}^4} \left(\frac{\mu_B}{\hbar}\right)^2 \int_{-\infty}^{+\infty} dq_y \frac{e^{-2qz}}{(\alpha(\alpha + q))^2} S_2(\mathbf{q}) \quad (25)$$

Here we have used $N\phi_0/(L_x L_y) = B$, where B is the flux density, $L_x L_y$ is the sample area and N is the number of vortices. To find the *total* excitation by the vortex lattice this result should be averaged over initial states and summed over final state.

Finally, we identify the average *rate* for the excitation process $g \rightarrow e$. This is given by the transition probability (25) divided by the time $\tau = L_x/v$ it takes an atom moving with velocity, v , to pass over the sample.

$$R_{ge}(v, z) = 2\eta_j |M_{eg}|^2 \frac{1}{\pi v} \frac{B\phi_0}{\lambda_{ab}^4} \left(\frac{\mu_B}{\hbar}\right)^2 \int_{-\infty}^{+\infty} dq_y \frac{e^{-2qz}}{(\alpha(\alpha + q))^2} S_2(\mathbf{q}), \quad (26)$$

-
- [1] P. L. Gammel et al., Phys. Rev. Lett. **59**, 2592 (1987).
 - [2] I. Maggio-Aprile et al., Phys. Rev. Lett. **75**, 2754 (1995).
 - [3] H. F. Hess et al., Phys. Rev. Lett. **62**, 214 (1989).
 - [4] K. Harada et al., Phys. Rev. Lett. **71** 3371 (1993).
 - [5] Goa, P. E. et al, Supercond. Sci. Tech. **14**, 729 (2001).
 - [6] A. Oral *et al.*, Phys. Rev. Lett. **80**, 3610–3613 (1998).
 - [7] S. J. Bending, Adv. Phys. **48**, 449 (1999).
 - [8] E. M. Forgan, D. McK. Paul, H. A. Mook, P. A. Timmins, H. Keller, S. Sutton, and J. S. Bell, Nature **343**, 735 (1990)
 - [9] S. Dapore-Schwartz, N. G. Woodard and G. P. Lafyatis, Phys. Rev. B **55**, 5655 (1997).
 - [10] H. Hauglin, N. G. Woodard and G. P. Lafyatis, submitted for publication.
 - [11] T. R. Brown and J. G. King, Phys. Rev. Lett. **26**, 969 (1971).
 - [12] G. J. Dolan et al., Phys. Rev. Lett. **62**, 2184 (1989).
 - [13] The signal could in principle be due to *two* orientations, related to one another by a mirror flip around the x-axis.
 - [14] S. T. Johnson et al, Phys. Rev. Lett. **82**, 2792 (1999).
 - [15] C. Ager et al, Phys. Rev. B **62** 3528 (2000).
 - [16] N. L. Wang, S. Tijima, A. I. Rykov, and K. Tomimoto, Phys. Rev. B **57** R11081 (1998); D. N Basov et al, Phys. Rev. Lett. **74**, 598 (1995).
 - [17] A. G. Sun *et al*, Phys. Rev. B **52**, R15731, (1995).
 - [18] R. Liang, P. Dosanjh, D. A. Bonn, D. J. Baar, J. F. Carolan and W. N. Hardy, Physica C **195**, 51 (1992).
 - [19] J. Giapintzakis, D. M. Ginsberg and P.-D. Han, J. Low. Temp. Phys. **77**, 155 (1989).
 - [20] N. Woodard, E. Hufstedler, and G. P Lafyatis, Appl. Phys. Lett. **64**, 1177 (1994); J. Fox , N. Woodard, and G. P Lafyatis, Rev. Sci. Inst. **70**, 1951 (1999).
 - [21] M. C. Marchetti, Physica C **200**, 155 (1992).
 - [22] C. Cohen-Tannoudji, J. Dupont-Roc, and G. Grynberg, *Atom-Photon Interactions*, J.Wiley & Sons, New York (1992).
 - [23] J. Ziman, Chapter 4, *Models of Disorder*, Cambridge University Press, 1979.

Figure Captions

FIG. 1. Principle behind Atomic Beam Magnetic Resonance. An atom travelling through the *spatially inhomogeneous* magnetic field above the surface of a type II superconductor in the mixed state will experience a *time-dependent* magnetic field. The frequency spectrum of that field depends on the spatial pattern of vortices and the velocity of the atom. If the magnetic field has a frequency component coincident with a magnetic dipole transition of the atom, that transition may be strongly driven. For a given transition, atoms travelling at different velocities will be sensitive to different *spatial* Fourier components of the inhomogeneous magnetic field. Therefore by measuring the transition probability for a particular transition *as a function of the atomic velocity*, we can study the spatial characteristics of the magnetic field associated with the flux line array and hence the structure of the vortex lattice itself.

FIG. 2. Zeeman manifolds for the relevant energy levels of ^{39}K . Shown are manifolds for the three lowest electronic states. Faint horizontal lines show nearby hyperfine states that are not *directly* used in the experiment. The energy scale is extremely distorted. Dashed lines indicate transitions that result from spontaneous emissions. The detection transition indicated is the cycling transition that is responsible for most of the fluorescence signal. The magnetic resonance (MR) transition that is driven by the vortex lattice, as discussed in the text, actually consists of nine allowed state-to-state excitations between the $F = 1$ and $F = 2$ levels. Similarly, the figure shows only one of the several state-to-state transitions transitions that are driven by the pumping laser.

FIG. 3. Experimental layout. The apparatus consist of three functionally distinct sections: (1) State preparation, where a thermal beam ($T \simeq 400^\circ \text{C}$) of potassium atoms is created and optically pumped into the $F = 1$ level; (2) A cryogenic sample region, where the atomic beam passes close to the surface of the superconducting sample in the mixed state and magnetic resonance transitions may be driven. For most of this work, the sample consists of a thin platelet of YBCO in a $\sim 10 \text{ G}$ field perpendicular to its surface (crystalline c -axis). (3) A detection region in which atoms that have been excited to the $F = 2$ manifold are detected as a function of their velocity. Excited atoms are detected *via* laser induced fluorescence. The Doppler shift of the laser driven transition is used to discriminate

atom velocities. Small signals and large backgrounds require an involved detection scheme, as described in the text.

FIG. 4. ABMR data acquired for different values of the bias field. Vortex lattices are created by “field cooling.” I.e. the sample is cooled through its transition temperature in the presence of the indicated bias magnetic field. These data were taken for $T = 10$ K. They show the expected trend: for stronger fields, vortices are closer together.

FIG. 5. Data for a sample in a field of 10.7 G. These data were acquired for a sample temperature of 10 K. For this case, the 10.7 G refers to the field actually measured by a miniature Hall probe array at the surface of the sample. The two peaks — at 1.24μ and 1.68μ — describe a triangular vortex lattice with sample wide order whose symmetry axes do *not* lie along the direction of the atomic beam.

FIG. 6. Triangular vortex lattices. The strongest peaks in ABMR spectra are due to the coherent excitation of atoms by rows of nearest neighbor vortices. For triangular lattices, there are three sets of such rows as shown on the figures. For each set of rows, a bar indicates the distance atoms travel between rows; these distances correspond to peaks in the spectra. Fig A) shows the case for the atomic beam traveling along a symmetry axis of the vortex lattice: this would create one sharp peak. Fig B) shows a vortex lattice that is tilted with respect to the atomic beam. Specifically, Fig B) shows a tilt, $\theta = 15^\circ$ — the orientation of the vortex lattice measured in FIG. 5. The dashed [dotted] rows produce the $d_1 = 1.68 \mu$ [$d_2 = 1.24 \mu$] peaks in that figure. At the top, a third peak is predicted but its distance is larger than the range of sensitivity of the present experiment.

FIG 7. Niobium data from “I.” The broad asymmetric peak is characteristic of a vortex lattice made up of randomly oriented domains within which there is short range translational order. The smooth curve is a model prediction for such a vortex lattice.

FIG. 8. A gallery of ABMR signals predicted for several forms of vortex matter. (A) Gas of uncorrelated vortices, (B) liquid with short range translational and orientational order, (C) Powder correlations due to randomly oriented vortex crystallites (D) Hexatic vortex glass with sample wide orientational order and short range translational order, oriented with a primitive lattice vector along the atomic beam. (E) is (D) rotated by 15° . (F) Excitation

due to a triangular near-crystalline vortex array with a primitive lattice vector oriented along the atomic beam.

FIG. 9. Representative raw experimental signals and reduced data. Experimentally, the top curves are measurements of laser induced fluorescence. The “pumped cold” data contain the signal and the “pumped warm” data are the background. The “unpumped distribution” is used to normalize the data and shows the sensitivity of our apparatus to different velocity classes of atoms. The velocity scale on the horizontal axis is determined from the Doppler shift of the detection laser and may be immediately converted to the distance scale of the other figures using $d = v/f$. By reducing the data, as discussed in the text, we directly measure the absolute excitation probability of the atoms by the vortex lattice.

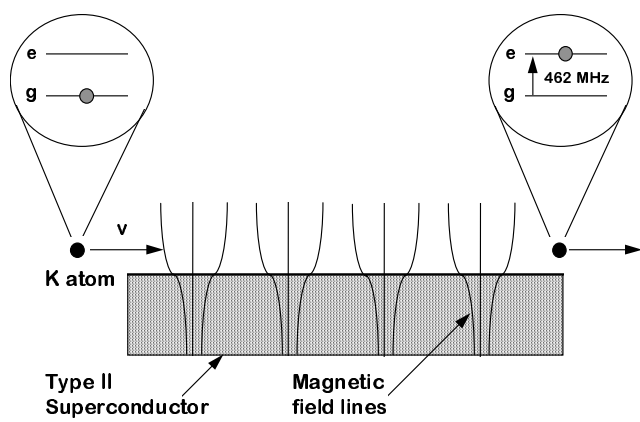
FIG. 10. Calculated first order excitation “probability” for atoms passing at different heights above a vortex lattice. The calculation is from the vortex lattice model that best reproduces the experimental data of FIG. 5. Note that essentially all of the signal comes from atoms passing within 1μ of the surface. The importance of including saturation effects in the modeling is seen where the first order theory predicts probabilities > 1 for atoms passing close to the surface

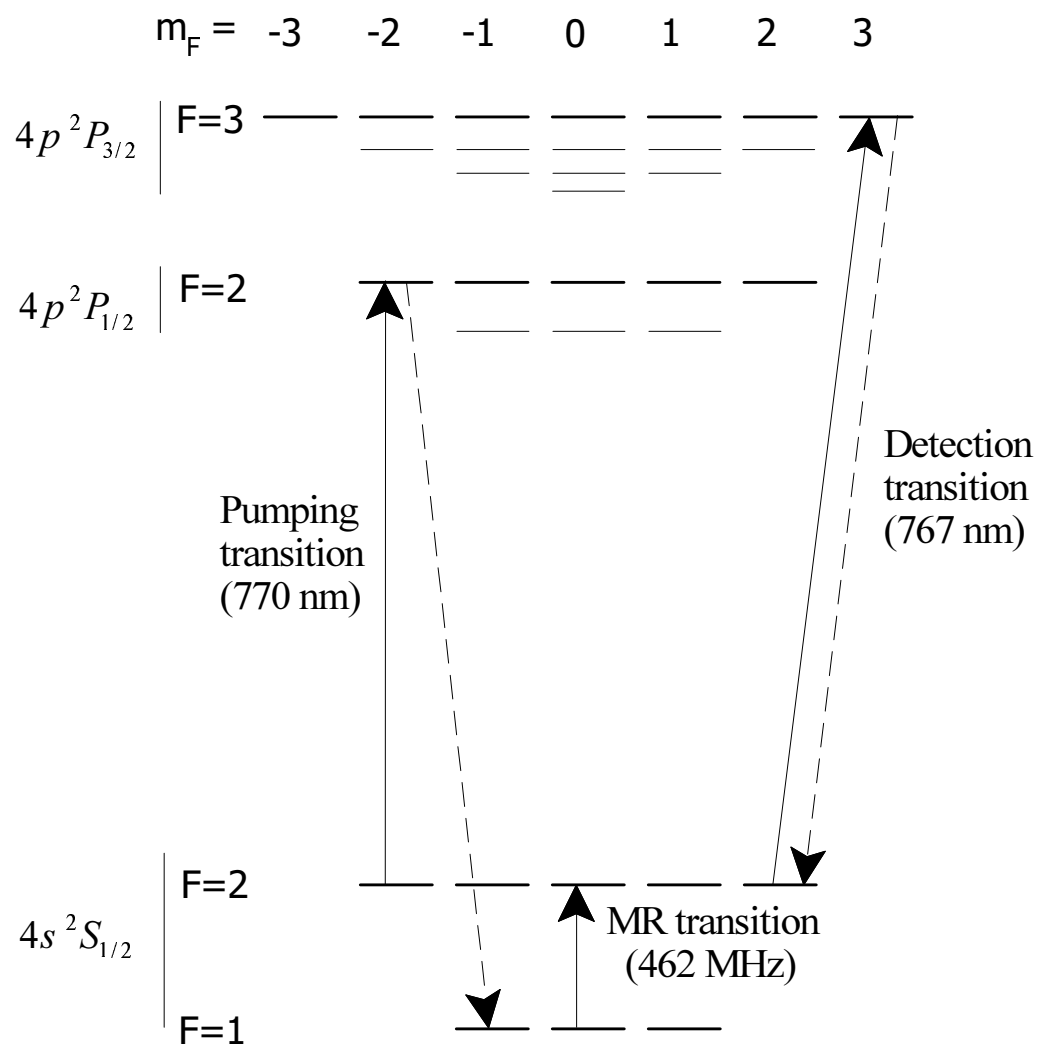
FIG. 11. Testing the two-level Master equation model by comparing it with an exact solution of the Schrödinger equation calculation. Calculations are done for 690 m/s atoms passing 0.2μ above a triangular lattice. The model lattice was disordered by adding to each vortex a random displacement, averaging 0.1 lattice spacings, from its nominal triangular lattice position. The jagged curve is a simulation in which the exact time dependent Schrödinger equation of the ground state hyperfine manifold is solved for 200 trajectories over the model vortex lattice. The smooth curve is the time integration of Eq. 10 — the model used in this work. By construction, the two-level Master equation model is *expected* to agree with the exact calculation in the perturbative and the fully saturated limits. Empirically in this and other comparisons, we find good agreement at *all* times. The exact solution took over 1000 times longer to run than the Master equation calculation.

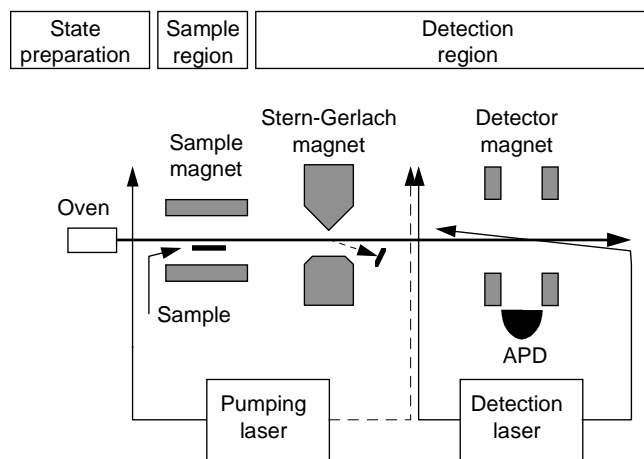
FIG.12. Contour plot of a model vortex pair distribution function. Deviations from perfect crystalline order is described by a Gaussian distribution with a separation dependent variance $\sigma(r) = \sigma_0(r/a_0)^p$, where $a_0 = \sqrt{\phi_0/B}$ is the average vortex spacing. The pair

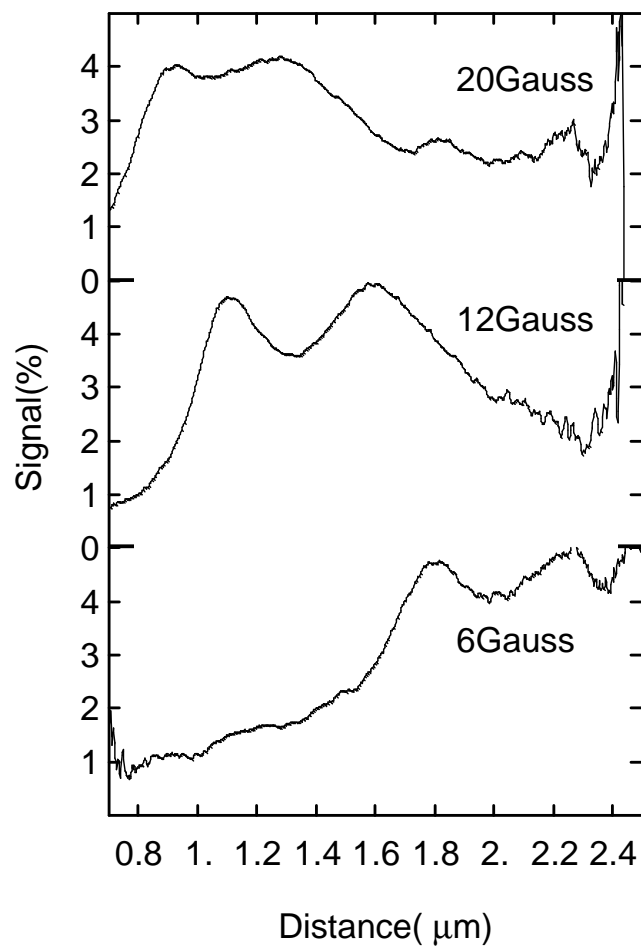
distribution shown is for $\sigma_0 = 0.14$ and $p = 0.5$. The unit cell is specified by the magnitudes of the primitive lattice vectors \mathbf{r}_1 and \mathbf{r}_2 , the angle θ that \mathbf{r}_1 makes with the atomic beam direction (x-axis) and the angle β between \mathbf{r}_1 and \mathbf{r}_2 .

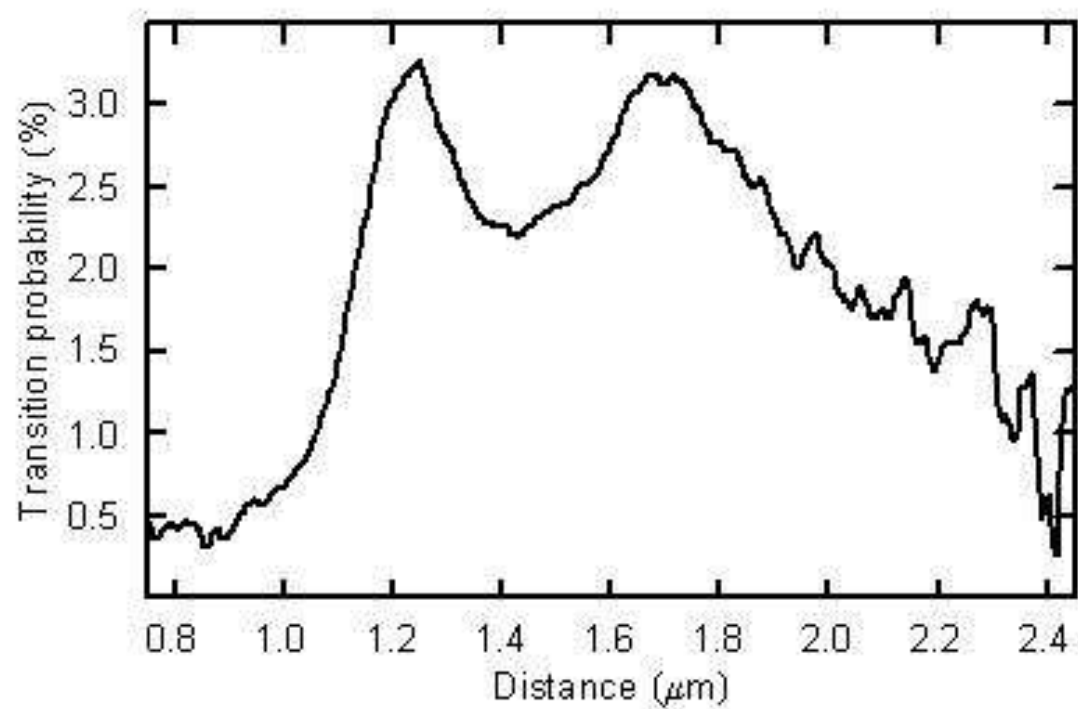
FIG 13. Best-fit model overlaying the data of FIG. 5. The best fit model lineshape (dark smooth line) is for a correlation function with $\sigma_{lm} = \sigma_0 x_{lm}^p$ where $p = 0.5$ and $\sigma_0 = 0.14a_0$. The overall signal strength is best fit assuming a penetration depth $\lambda_{ab} = 140$ nm. The upper curve and lower lighter curves show model predictions for penetration depths of 100 nm and 180 nm, respectively.



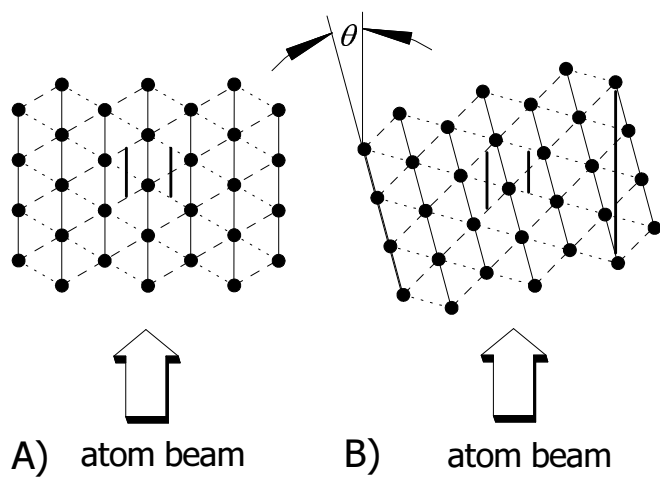




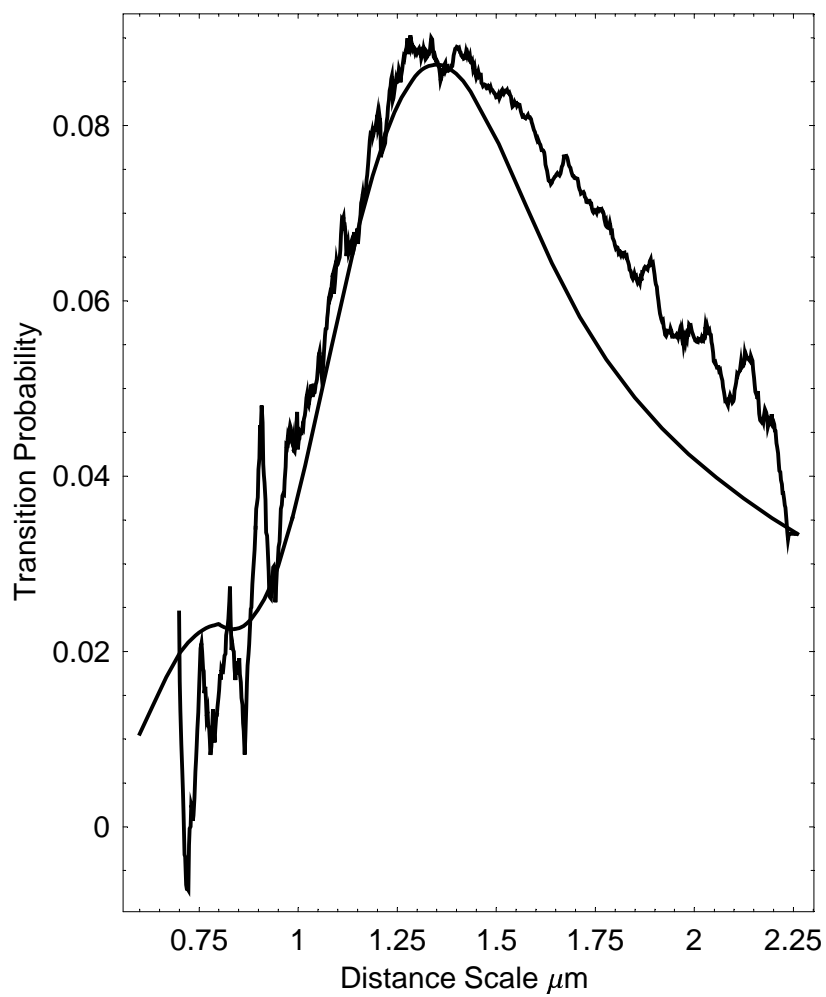


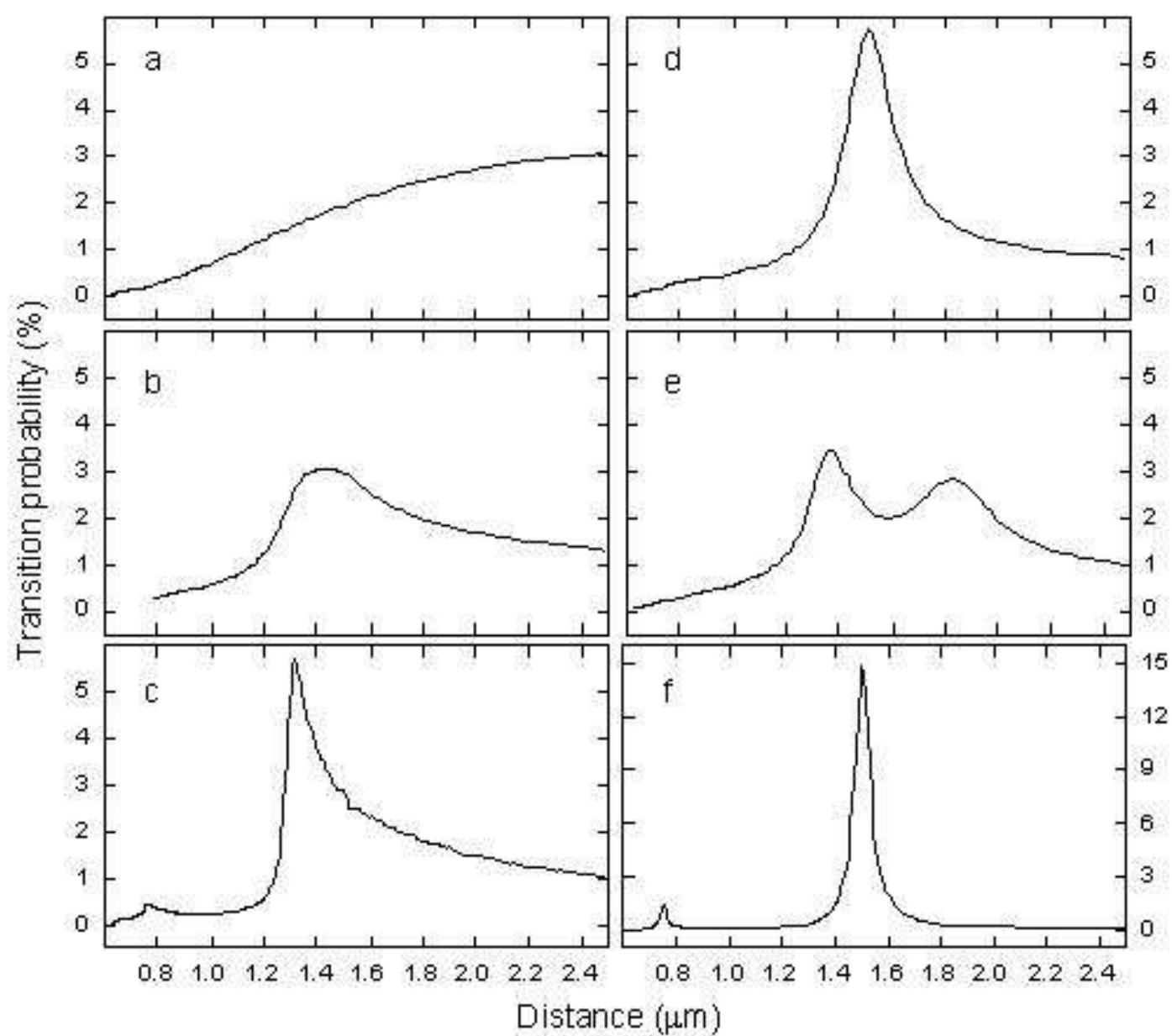


H. Hauglin
Fig. 5

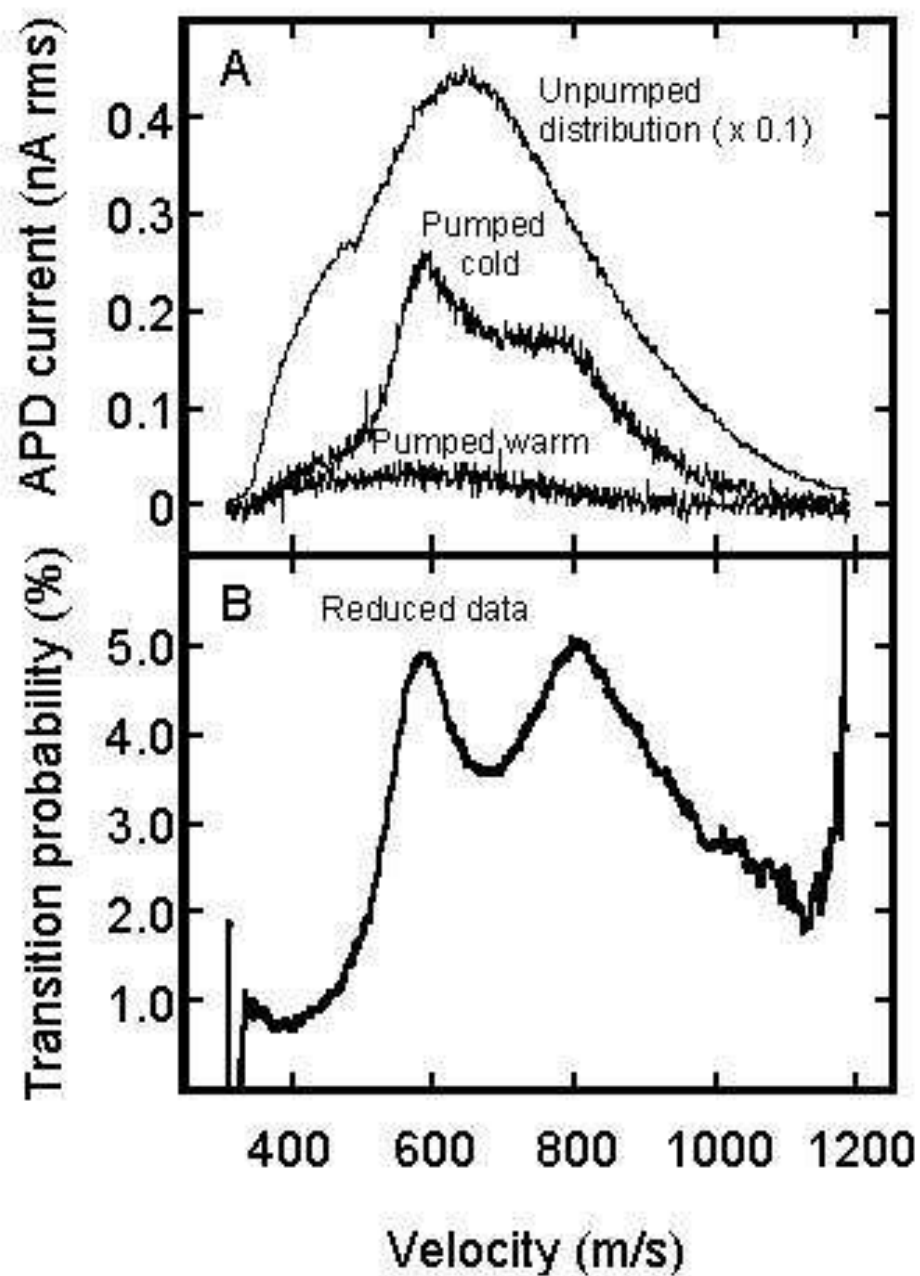


Niobium film in a 13.5 G field

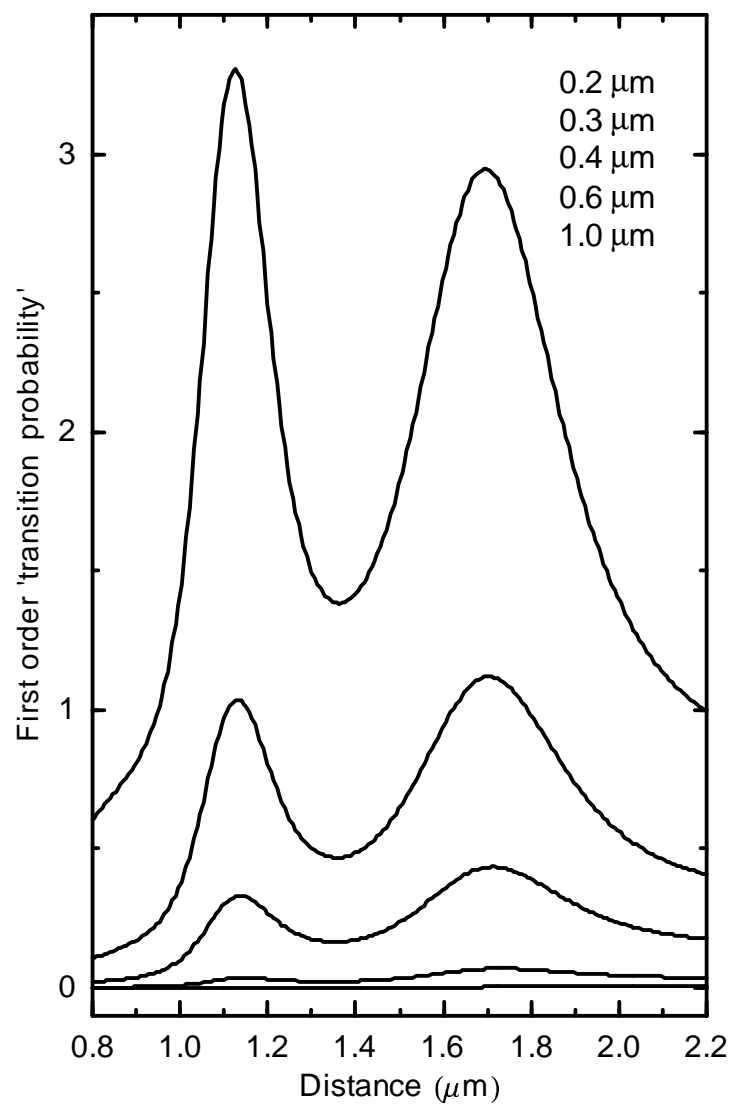


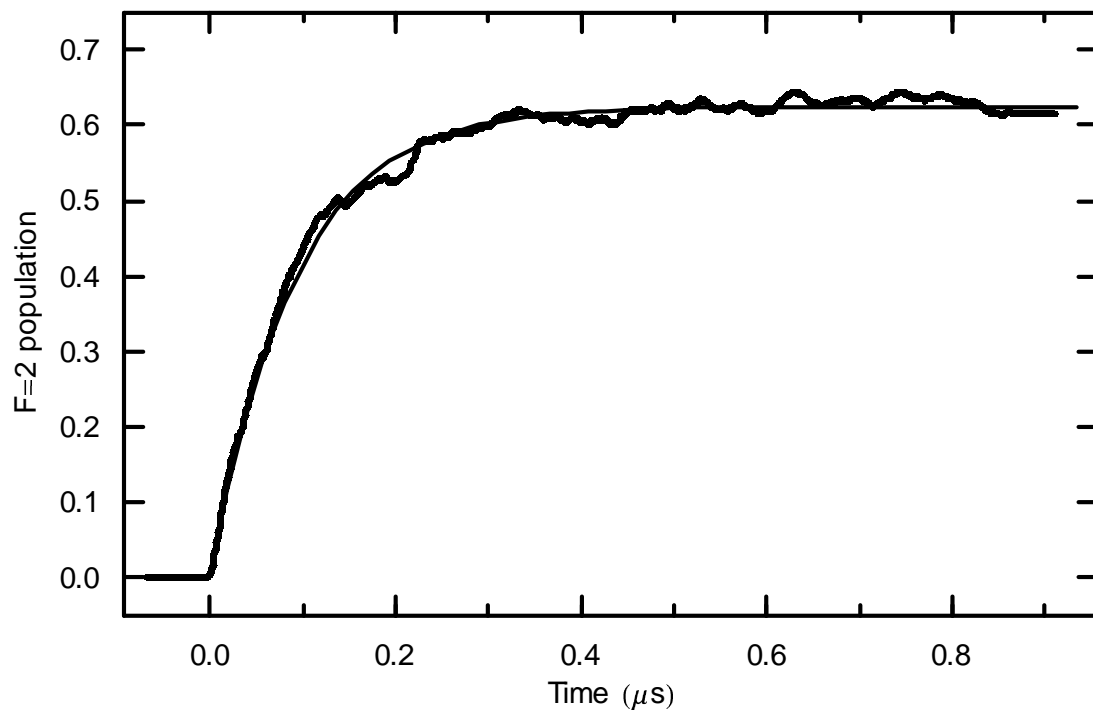


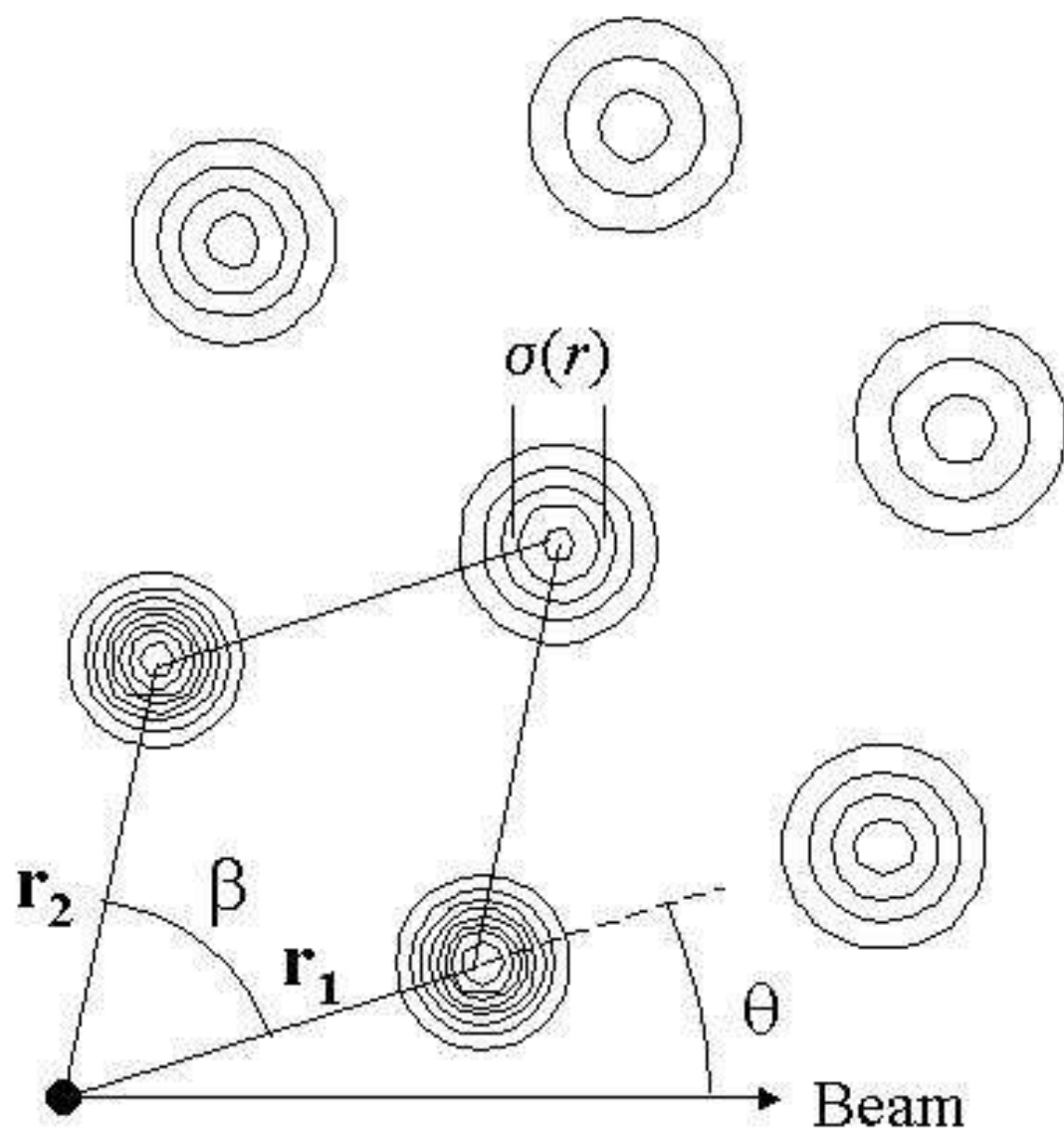
H. Hauglin
Fig. 8



H. Hauglin
Fig. 9







H. Hauglin
Fig. 12

